Dense cores in the L1630 molecular cloud: discovering new protostars with SCUBA

Robin R. Phillips[1][*], Andy G. Gibb[2][†] and Leslie T. Little[1]

[1] *Electronic Engineering Laboratory, University of Kent at Canterbury, Canterbury, CT2 7NT*
[2] *Department of Physics and Astronomy, University of Leeds, Leeds, LS2 9JT*

ABSTRACT

Maps of the 450 μm and 850 μm dust continuum emission from three star-forming condensations within the Lynds 1630 molecular cloud, made with the SCUBA bolometer array, reveal the presence of four new submillimetre sources, each of a few solar masses, two of which are probably Class I, two Class 0, as well as several sources whose existence was previously known. The sources are located in filaments and appear elongated when observed at 450 μm. They likely have dust temperatures in the range 10 to 20 K, in good agreement with previous ammonia temperature estimates. Attempts to fit their structures with power-law and Gaussian density distributions suggest that the central distribution is flatter than expected for a simple singular isothermal sphere.

Although the statistics are poor, our results suggest that the ratio of 'protostellar core' mass to total virial mass may be similar for both large and small condensations.

Key words: stars: formation – radio continuum: ISM – ISM: clouds – ISM: individual: L1630 – ISM: individual: Orion B

1 INTRODUCTION

The Orion molecular clouds are the subject of extensive investigation on account of their proximity (400–500 pc) and the formation within them of stars of a variety of masses. An important unbiased survey of molecular condensations within the clouds is that of Lada, Bally and Stark (1991; hereafter LBS), who mapped the Orion B (L 1630) cloud with an angular resolution of 1.7 arcmin, observing emission from the J=2–1 transition of interstellar CS. Excitation of this transition requires molecular hydrogen densities of order 10^4–10^5 cm^{-3}. Several of these condensations have themselves been mapped with substantially higher resolution and in molecular transitions requiring still higher densities for excitation (Zhou et al. 1991; Lis, Carlstrom & Phillips 1991; Chandler, Moore & Emerson 1992).

Gibb & Heaton (1993; hereafter GH93) and Gibb et al. (1995; Paper I) mapped 6 of the LBS condensations in the J=3–2 or J=4–3 transitions of interstellar HCO$^+$. These revealed an apparently filamentary structure containing embedded cores whose virial masses were typically a few solar masses.

Paper I mapped the dust continuum emission from several of the cores in LBS23, while Gibb & Little (1998; hereafter GL98)

mapped the whole of LBS23 in J=2–1 C^{18}O. Dust-derived masses for the cores were in good agreement with their virial masses derived from HCO$^+$. The emission peaks evident in HCO$^+$ usually correlated well with those of the dust continuum but were faint or missing in C^{18}O. GL98 considered that these results implied depletion of the C^{18}O by factors of between 10–50. The lack of correlation between dust continuum and C^{18}O was similar to that found in the hotter source NGC2024 (Mauersberger et al. 1992). The simple interpretation as depletion in NGC2024 (Mezger et al. 1992) has been questioned by Chandler & Carlstrom (1996) on the grounds that (a) the dust opacity law in the cores may be non-standard, (b) dust emission may become optically thick at the short submm wavelengths, but erroneously interpreted as thin, (c) the cores may contain unresolved components which are highly optically thick in C^{18}O but interpreted as thin so the true molecular abundance is much higher.

The recent availability of the Submillimetre Common User Bolometer Array (SCUBA: Holland et al. 1999) permits rapid mapping of dust emission from the LBS condensations with greatly improved sensitivity. This means that large areas within them can be mapped to determine the gross dust distribution and further protostellar cores may be readily identified. We here describe the results of a pilot study in which selected areas of our LBS condensations have been mapped with SCUBA.

The motivation for this study was:

(a) to search for dust components near, for example, outflow
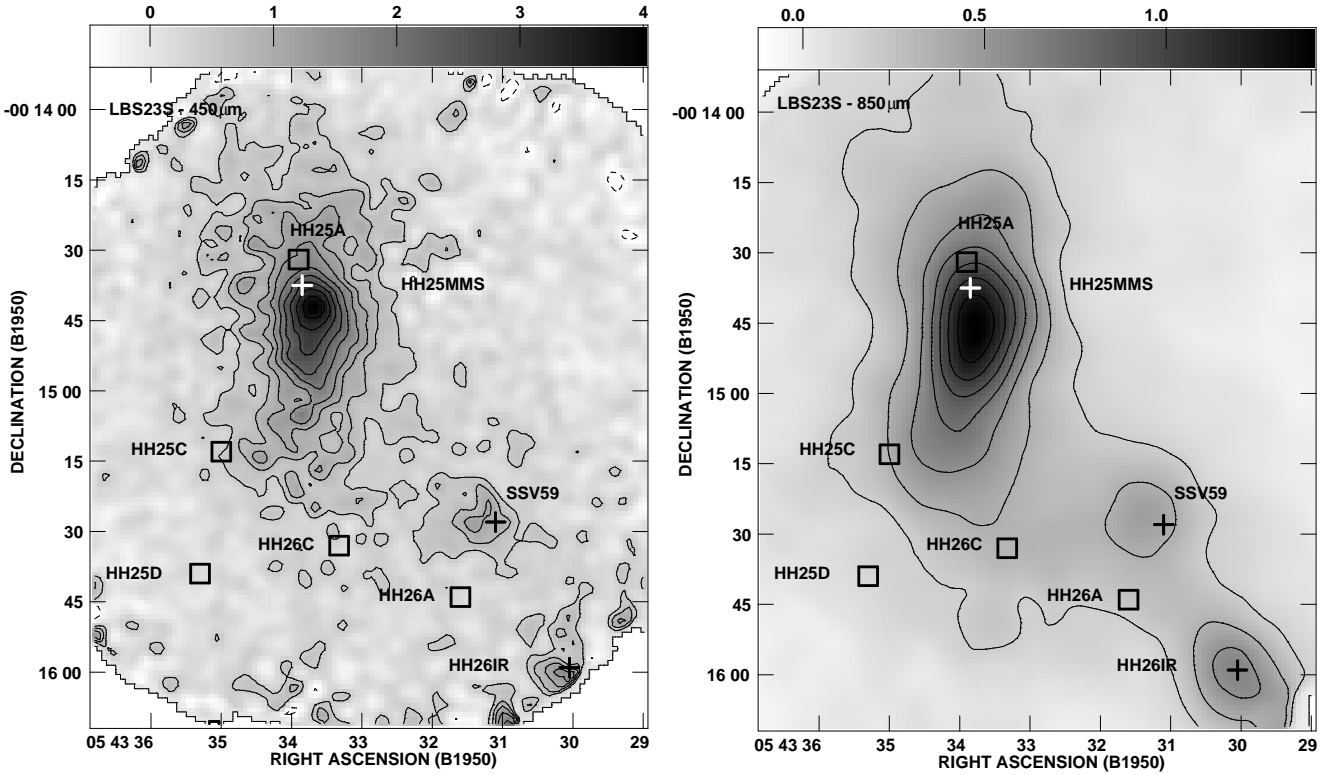
Figure 1. SCUBA maps of LBS23S at 450 μm (left) and 850 μm (right). The known sources HH25MMS, SSV59 and HH26IR are marked by crosses, while the components of HH25 and HH26 from Davis et al. (1997) are marked by open squares. The greyscale is in Jy/beam and is shown as a bar across the top of each figure, extending from -3σ to the maximum (4.0 Jy/beam at 450 μm and 1.4 Jy/beam at 850 μm). Contours are -3, 3, 5, 7, 9, 12, 15, 18, 21, 24 (450 μm) and 5, 10, 15, 20, 25, 30, 35, 40 (850 μm) times the noise level of 150 mJy per beam and 36 mJy per beam respectively.

sources, near-infrared sources, and Herbig-Haro objects, where they have not previously been detected, and for new protostellar objects.

(b) to compare the observed dust emission with models of the structure of protostellar cores such as those of Shu (1977), or Crutcher et al. (1994). The simultaneous mapping of the cores at 850 and 450 μms facilitates some separation of dust mass and temperature.

(c) to see whether the morphology of large scale filaments fragmenting into protostellar cores evident in e.g. NGC2024 and LBS23 extends to smaller condensations.

(d) to compare the numbers of protostellar cores in large and small condensations in the same molecular cloud and to see if stars form preferentially in the larger condensations.

(e) to map fields for which detailed HCO$^+$ and C^{18}O maps exist already, to determine molecular depletion in different source components. A detailed analysis will follow in a later paper.

2   OBSERVATIONS

The observations were made using the submillimetre bolometer array receiver SCUBA (Holland et al. 1999) operated in service mode at the James Clerk Maxwell Telescope over the period 24 to 26 August 1997 and 20 and 23 September 1997. The 32 element 850 μm and 96 element 450 μm arrays were used in 'jiggle-mode' to make fully-sampled maps of 2.2-arcmin diameter-fields in 6 of the LBS cores. The chop throw was 120 arcsec in azimuth. The flux scales were established by observations of Uranus at the start of each ob-

serving session and skydips were used to calculate the zenith optical depth at the start and end of each session.

The night of 26 August was very humid and calibration produced results that differed by of order 50 per cent (lower) compared with the previous and following nights. The weather on the nights of 20 and 23 September was poor and the 450 μm data could not be used. Thus the images presented were constructed from data recorded on the nights of 24 and 25 August 1997 only. On these two nights, the estimated calibration uncertainty is of order 10 per cent at 850 μm and 30 per cent at 450 μm. The beam of the telescope was determined to have full-width at half-maximum (FWHM) diameter of 15.0$\pm$0.5 arcsec at 850 μm and 8.1$\pm$0.2 arcsec at 450 μm. The total time on each source was of order one hour, except for LBS7, 13 and 16. Due to poor weather the time on source for these fields was only 21 minutes.

The typical noise level at 850 μm and 450 μm was 34 mJy per beam and 150 mJy per beam respectively for LBS17, 18 and the two fields in LBS23. This translates to a 3σ mass sensitivity of 0.6 M$_\odot$ for temperatures of 10 K, assuming that the dust emissivity is as described by Hildebrand (1983). The noise level for LBS7, 13 and 16 was higher at $\sim$80 mJy per beam at 850 μm; no emission was detected in these fields.

Table 1 summarises the fluxes and positions of the dust emission sources detected in the LBS cores.
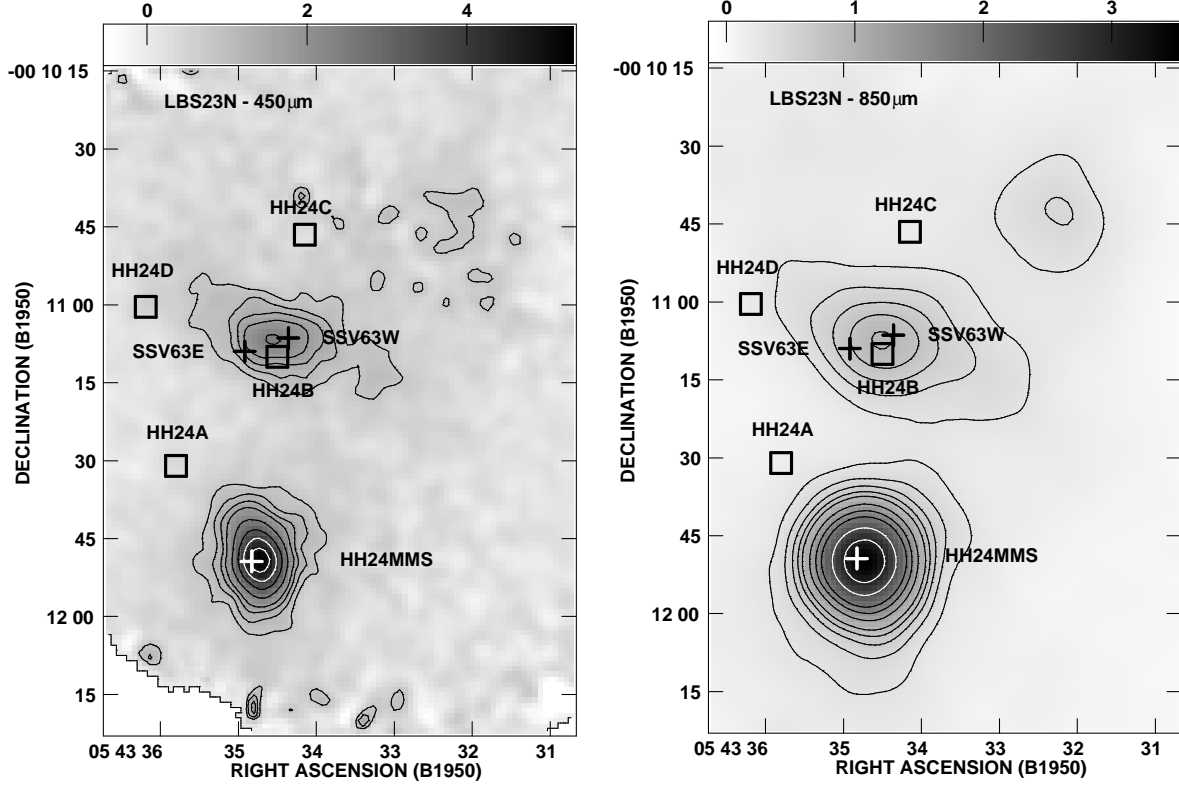
Figure 2. SCUBA maps of LBS23N at 450 μm (left) and 850 μm (right). The known sources HH24MMS, SSV63E and SSV63W are marked by crosses while the Herbig-Haro objects HH24A–D are marked by open squares. The greyscale is in Jy/beam and is shown as a bar across the top of each figure, extending from -3σ to the maximum (5.3 Jy/beam at 450 μm and 2.5 Jy/beam at 850 μm). Contours are –3, 3, 5, 7, 9, 11, 15, 20, 25, 30 (450 μm) and 10, 15, 20, 25, 30, 40, 50, 60, 80, 100 (850 μm) times the noise level of 160 mJy per beam and 30 mJy per beam respectively.
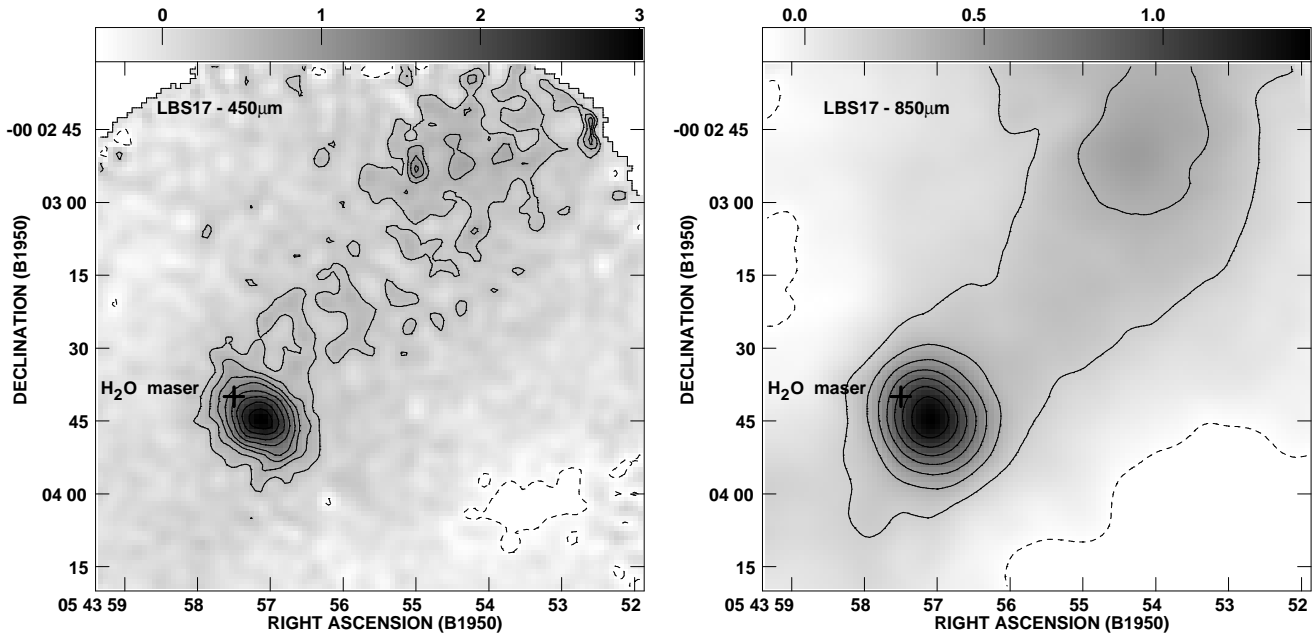
Figure 3. SCUBA maps of LBS17 at 450 μm (left) and 850 μm (right). The water maser of Haschick et al. (1983) is marked by a cross. The greyscale is in Jy/beam and is shown as a bar across the top of each figure, extending from -3σ to the maximum (3.0 Jy/beam at 450 μm and 1.4 Jy/beam at 850 μm). Contours are –3, 3, 5, 7, 9, 12, 15, 18, 21, 24 (450 μm) and –3, 5, 10, 15, 20, 25, 30, 35, 40 (850 μm) times the noise level of 130 mJy per beam and 35 mJy per beam respectively.
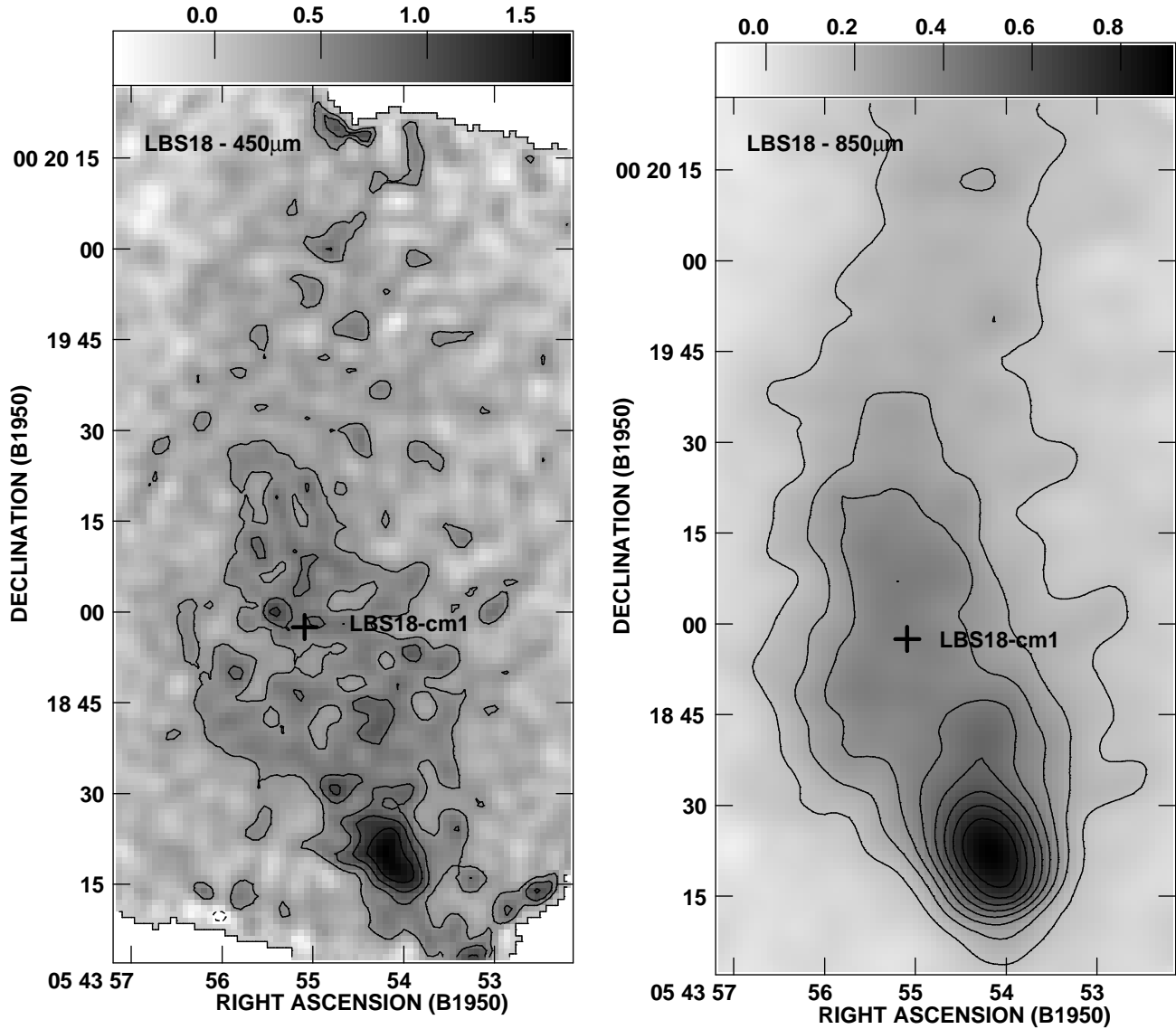
Figure 4. SCUBA maps of LBS18 at 450 μm (left) and 850 μm (right). The 3.5-cm source detected by Gibb (1999) is marked by a cross. The greyscale is in Jy/beam and is shown as a bar across the top of each figure, extending from -3σ to the maximum (1.7 Jy/beam at 450 μm and 0.91 Jy/beam at 850 μm). Contours are –3, 3, 5, 7, 9, 12, 15, 18, 21 (450 μm) and 5, 8, 11, 14, 17, 20, 23, 26 (850 μm) times the noise level of 150 mJy per beam and 33 mJy per beam respectively.

3   RESULTS

Figs. 1 to 4 show the SCUBA maps at 450 and 850 μm for the four LBS fields in which emission was detected. Table 1 lists the parameters derived from two-dimensional gaussian fits (using the task IMFIT in AIPS) for the sources detected in the LBS17, 18 and 23 fields. The source dimensions have not been deconvolved. The (formal) uncertainties in the positions and dimensions arising from the fitting procedure are of order 0.5 arcsec. The main features of each source will now be discussed in turn.

3.1   LBS23S

This field is centred on the class 0 source HH25MMS (Gibb & Davis 1998) and contains the class I infrared sources SSV59 and HH26IR (Davis et al. 1997). The purpose of mapping this region was to compare the SCUBA maps of HH25MMS (Fig. 1) with

the existing UKT14 map (Paper I) and also to search for the driving source of the southern bipolar outflow in HH24-26 (GH93). The morphology of HH25MMS is consistent in both maps, and the maximum lies within a couple of arcsec of the 3.4-mm peak of Choi et al. (1999). Two further weaker components are evident in Fig. 1; they are associated with HH26IR, which is the source of the southern outflow (GH93), and SSV59, which also drives a molecular outflow (Gibb & Davis 1997). Edge effects make it difficult to make accurate measurements of the flux density of HH26IR as we have not observed the entire source. Recent 1300-μm and 350-μm observations of the whole of LBS23 by Lis, Menten & Zylka (1999) reveal a structure consistent with what we observe in Figs. 1 and 2. They show that HH26IR also appears to be embedded within a clump elongated perpendicular to the CO flow.

A curious point is that the radio continuum source and origin for the HH25MMS molecular outflow is not coincident with the

submillimetre continuum peak, being offset by ∼6 arcsec in declination, somewhat larger than the mean pointing error (3 arcsec). If genuine, this observation may indicate the presence of a second submillimetre source within LBS23S, which may be younger than HH25MMS (on account of there being no observable outflow). Alternatively, it may be a hot-spot heated by the impact of the outflow from HH25MMS. Clearly higher resolution observations are needed to clarify this issue. Lis et al. (1999) observe this in their 1300-μm map, but it seems less pronounced in their 350-μm data.

3.2 LBS23N

This field is centred on the HH24 complex, and includes the class 0 protostar HH24MMS. The two components HH24MMS and SSV63W detected at 1300 μm by Chini et al. (1993) are clearly mapped (Fig. 2). There is good agreement between the 850 μm SCUBA and 800 μm UKT14 (Paper I) peak fluxes for the unresolved source HH24MMS. The 450 μm map reveals the source to be extended in a N–S direction. While the flux densities are also in good agreement with the UKT14 data of Ward-Thompson et al. (1995) the SCUBA 450 μm observations show the source as much more compact. We note that the direction of the compact jet discovered by Bontemps, Ward-Thompson & André (1996) is neither parallel nor perpendicular to the elongation at 450 μm. A new weak source is seen 40 arcsec north-west of SSV63 which shows up weakly at 450 μm as well. We label this clump HH24NW (Table 1) although its parameters are not particularly well determined. Lis et al. (1999) also detect this source.

3.3 LBS17

Fig. 3 presents the submillimetre map of the south-eastern portion of the HCO$^+$ ridge of Paper I. The J=3–2 HCO$^+$ map produced a peak largely missing in C^{18}O (Paper I; Gibb & Little 2000). However, this peak stands out as a dust source in the SCUBA map. There is a bipolar outflow associated with this source, observable in HCO$^+$ and CO (Gibb & Little 2000). The elongation of the dust source, observable at 450 μm, is perpendicular to the direction of the bipolar outflow. No IRAS, optical or near-infrared emission appears to be associated with the source – so it is likely to be young, possibly protostellar. Gibb & Little (2000) showed that it satisfies the criteria for being a class 0 candidate. We refer to this source as LBS17H, to distinguish it from another source detected in the LBS17 condensation to the north of the area covered by our map by Launhardt et al. (1996). This second source lies near a peak of our HCO$^+$ map (Paper I). A ridge of dust emission (Fig. 3) is perceived to run NW towards an extended plateau leading on to this peak, a feature also evident in HCO$^+$. A poorly-defined peak is seen in the northwest of the 850-μm image although this may be an artefact of the mapping procedure. However, it is coincident with one of the HCO$^+$ clumps of Paper I, clump B6 although in keeping with the revised nomenclature we label it LBS17F in Table 1. A more extensive map is required to determine its true parameters.

3.4 LBS18

LBS18 has one of the smallest virial masses of the LBS cores (14 M$_\odot$). In dust emission (Fig. 4), as in J=3–2 HCO$^+$ (Paper I) and J=2–1 C^{18}O (Little et al., in prep), the source has a 'cometary' appearance, showing a N–S elongation with a compact component at one end, which could be protostellar. Gibb (1999) detected a

Table 2. Masses derived from simple isothermal analysis assuming a temperature estimated from previous NH$_3$ data and an emissivity index of 2. The mass within 8 arcsec was calculated from the 450 μm flux density; that within 15 arcsec from the 850 μm flux density. The Class label is that defined by Lada (1991) and updated by André, Ward-Thompson & Barsony (1993).

Source	$T_{\rm d}$ (K)	M (M$_\odot$) (8 arcsec)	M (M$_\odot$) (15 arcsec)	Class	Outflow
LBS17H	15	0.9	2.1	0	Y
LBS18S	15	0.5	1.4	?	N?
HH25MMS	18	0.8	1.6	0	Y
SSV59	18	0.2	0.5	I	Y
HH24MMS	12	2.9	7.9	0	Y
SSV63	12	1.3	2.3	I	Y

radio continuum source within this core using the VLA but it lies within the main north-south ridge, and is not coincident with the compact component.

4 ANALYSIS

4.1 Simplest model – spherically-symmetric, isothermal cores

To determine the mass and temperature of the clumps requires a knowledge of the emissivity law, and that the distribution of emission should be well resolved and observed with high signal-to-noise ratio at at least two different wavelengths. These conditions are not satisfied for our observations. The emissivity law is uncertain and even if this were not the case uncertainty in calibration (dominated by the 450 μm measurements) would be a strongly limiting factor in fixing the temperature and hence the mass. The clumps are barely resolved and the temperature within them may well vary with position, so that only an oddly weighted beam average can be derived. How then are we to proceed?

Initially we have assumed the clumps possess the simplest possible structure. They were assumed to be optically thin and at a constant temperature, which we obtain from previous ammonia observations (Menten, Walmsley & Mauersberger 1987; Verdes-Montenegro & Ho 1996). Where no prior temperature data exist we have assumed an intermediate value of 15 K. Better estimates of the dust temperature may be obtained from greybody fitting if enough data exist. We employed the Hildebrand (1983) emissivity value of 0.1 cm^{2}g^{-1} at 250 μm to estimate the appropriate values at 850 μm and 450 μm assuming a value of β of 1.5, the median value typical of dust emission in dense cloud cores (e.g. Huard, Sandell & Weintraub 1999; Chandler & Richer 2000). The core mass is given by $F_\nu d^2/(\kappa_\nu B_{\nu,T})$ where F_ν is the flux density at frequency ν, d is the distance to the source, κ_ν is the absorption coefficient and $B_{\nu,T}$ is the Planck function for a blackbody of temperature T.

Even if these assumptions closely model reality, the calibration error alone limits the determination of mass to within 50 to 100 per cent. The assumed temperatures and derived masses are shown in Table 2. Despite the uncertainties, it seems that the dust cores probably have a mass within a 0.03 pc diameter region of order 1–2 M$_\odot$. The mass derived for HH24MMS seems anomalously high, which led Chini et al. (1993) to suggest that the absorption coefficient is larger towards this source (possibly due to a lower value for β or a coagulation of dust grains).

We have made greybody fits to the spectral energy distribu-

Table 1. Source parameters, including identification where known. The source dimensions were derived from 2-dimensional gaussian fits and list the FWHM of the major and minor axes (in arcsec) and the position angle of the major axis in degrees east of north. Angles are rounded to the nearest integer. The last three columns list the flux density (in Jy) within an aperture of either 8 or 15 arcsec.

LBS core	Source	Source Position RA(1950.0), Dec(1950.0)	$a_{850} \times b_{850}$ arcsec^2	PA degrees	$a_{450} \times b_{450}$ arcsec^2	PA degrees	$F(8'')$ 450 μm	$F(15'')$ 850 μm	450 μm
17	LBS17H	$05^{\rm h}43^{\rm m}57.1^{\rm s}$, $-00°03'44.3''$	18×16	26 ± 2	12×9	49 ± 3	3.0	1.4	5.4
17	LBS17F	$05^{\rm h}43^{\rm m}54.2^{\rm s}$, $-00°02'48.2''$	32×23	-27 ± 3	–	–	–	0.4	–
18	LBS18S	$05^{\rm h}43^{\rm m}54.2^{\rm s}$, $+00°18'23.1''$	26×20	22 ± 4	14×10	31 ± 3	1.7	0.9	3.5
23	HH25MMS	$05^{\rm h}43^{\rm m}33.8^{\rm s}$, $-00°14'46.5''$	29×15	-8 ± 1	15×13	-1 ± 9	3.7	1.4	8.7
23	SSV59	$05^{\rm h}43^{\rm m}31.4^{\rm s}$, $-00°15'27.3''$	25×22	13 ± 6	11×10	79 ± 43	1.1	0.4	2.2
23	HH26IR	$05^{\rm h}43^{\rm m}30.1^{\rm s}$, $-00°16'00.1''$	27×17	42 ± 2	9×8	-57 ± 64	1.4	0.6	–
23	HH24MMS	$05^{\rm h}43^{\rm m}34.7^{\rm s}$, $-00°11'48.8''$	17×16	2 ± 5	13×9	9 ± 2	5.1	3.5	9.6
23	SSV63	$05^{\rm h}43^{\rm m}34.4^{\rm s}$, $-00°11'07.3''$	23×17	63 ± 5	16×10	79 ± 3	2.4	1.0	5.1
23	HH24NW	$05^{\rm h}43^{\rm m}32.3^{\rm s}$, $-00°10'43.1''$	24×21	21 ± 7	–	–	–	0.5	–

Table 3. Best fit parameters for Gaussian (columns 2–7) and power-law (columns 8–11) oblate models for each object modelled. Note that the mass estimates have been corrected for helium by multiplying the H$_2$ results by 1.25. For the Gaussian model $c_{\rm n}$ represents the maximum density and $d_{\rm n}$ and $e_{\rm n}$ the radii (to 1/e) on the major and minor axes. For comparison, the HWHM beam radius at 450 micron is 0.008pc. The $i_{\rm z}$ and $i_{\rm r}$ columns show the indices for the power law n$_{\rm H_2}$ distribution in each direction (i.e. when $\theta = \pi$ and $\theta = 0$ respectively in equation A3). $c_{\rm n}$ is then the density at the inner cut-off radius 0.001pc. The temperature distribution has been assumed to be spherically symmetric and varies according to $T_{\rm K} = a_T R^{0.3} + b_T R^{-0.3}$ where R is the distance to the centre of the cloud measured in parsecs, a_T being zero for the power law models.

Object	Mass (M$_\odot$)	Density c_n (cm^{-3})	Scale d_n (pc)	e_n (pc)	Temperature (K) a_T	b_T	Density c_n (cm^{-3})	Index i_z	i_r	Temperature (K) b_T
LBS17H	16	2.4×10^7	0.014	0.010	10	1.6	1.1×10^8	-1.4	-1.2	2.2
LBS18	21	9.8×10^6	0.025	0.010	0	2.1	2.3×10^8	-1.7	-1.3	1.7
HH24MMS	50	2.6×10^8	0.009	0.007	15	1.0	5.6×10^8	-1.6	-1.2	1.9
HH25MMS	12	1.4×10^6	0.045	0.018	5	4.3	1.3×10^7	-1.1	-0.7	3.9
SSV63	8	1.9×10^6	0.030	0.015	10	2.9	3.0×10^7	-1.6	-1.3	3.0

tions using our SCUBA and IRAS HiRes-processed data to place an upper limit on the dust temperature (see Gibb & Little 2000, Gibb & Davis 1998 for greybody fits to two of our SCUBA sources). In general this temperature lies between 20 and 30 K, depending on the value of β for the fit, with the clumps containing IRAS point sources tending to have higher upper limits than those dust clumps with no IRAS point source. Unfortunately the greybody fits cannot provide more accurate estimates of the temperature because the IRAS fluxes are measured with a beam considerably larger than that of our JCMT observations, one which often encompasses more than one of our SCUBA clumps.

If a power law variation of density with radius were assumed and the temperature constant this would imply a power-law index of –1.7, a value intermediate between the value expected for a singular isothermal sphere in hydrostatic equilibrium (–2) and one in free-fall collapse (–1.5). If temperature increases inward the power law would be flatter. If a Gaussian distribution is assumed, an angular diameter for the sources ~12 arcsec (0.023 pc) is indicated, probably too close to the SCUBA beamsize to be meaningful.

4.2   More detailed modelling of the emission

Although the data indicate that the observations have only partially resolved most of the sources (particularly in the narrow direction) the existence of simultaneously observed well registered maps at both 850 and 450 μms justified more detailed modelling which would be capable of taking into account density and temperature gradients and finite optical depth. In particular we wished to compare the predictions of both Gaussian and power-law models, as

they represent popular paradigms for the structure of such objects. We might attempt to distinguish between power law and Gaussian distributions by fitting the 850 μm and 450 μm observations *simultaneously*.

Accordingly, we have written a program that computes fluxes for model clouds with axial symmetry, described in the Appendix. To compare the model output with the telescope data two cuts were made on each of the SCUBA maps, one down the long axis of the cloud and one perpendicular to this. These cuts were then repeated on the model output and the results compared. The best fit oblate Gaussian and power law models for each object modelled are presented in Table 3. Given the uncertainties in the calibration, which will directly propagate into the magnitude of the density and temperature in the model, we emphasize that in this section we seek to explore the possible forms of the density variation, rather than absolute values.

We tried both the Hildebrand (β=2) and Testi and Sargent (1998) (β=1.1) versions of the emissivity function (see Appendix) to see whether the choice of β affects our results significantly. For the Gaussian distribution there is no significant observable change in the any of the output cross-sections. However, it is necessary to decrease the density by a factor of approximately 2 and increase temperature by a factor of approximately 1.5 in order to retain the correct intensities which has the result of decreasing the mass of the cloud by around 50 per cent. Therefore there does not seem to be any clear way of distinguishing between different values of β using this data set.

We have also investigated the differences caused by assuming an oblate or a prolate spheroid as the cloud shape. Unfortunately

there does not seem to be any way of distinguishing between the two models as the best fit line profiles are virtually identical in both cases. However, the parameters needed to obtain the best fit are significantly different. The Gaussian prolate case needs a higher density by a factor of between 1.3 and 3 (the more elliptical the cloud, the larger the difference). This in turn causes a higher cloud mass (up to 15 per cent). There is also a corresponding slight decrease in the temperatures required. All other parameters remain the same. For the power law distributions the same comments apply except that the increase in density caused a larger increase in the cloud mass (up to 50 per cent).

4.2.1 Features of the modelling

The results of the model fits are given in Table 3. In attempting the fits it was found that:

(1) At least two of the sources (LBS18S and HH25MMS) showed evidence for two or more components along their major axes.

(2) There was usually evidence of extended 'ridge' or 'wing' emission (up to 25 per cent of the peak) which could not be accounted for in the modelling carried out here.

(3) Gaussian fits are usually slightly better than power laws in one significant respect, described below.

Fig. 5 shows the fits for LBS17. The presence of a ridge connecting the main clump to a secondary clump to the north west causes an extended low level emission wing in the 850 μm x-axis cut which no effort has been made to fit. Ignoring this, the central part of the x-axis cut and the whole of the y-axis cut is almost perfectly fit by a Gaussian distribution profile. By contrast we were unable to find a power law fit that successfully modelled both the 450 μm and 850 μm maps *simultaneously*.

For power laws the 850 μm y-axis cut cannot be made narrow enough without causing the 450 μm y-axis cut to become too narrow. The smaller 450 μm beam weights the central material more heavily – too heavily for the inwardly increasing power law.

Of the five sources which were modelled this feature was observed along the major axes of SSV63, LBS17H, and LBS18S, and the minor axes of HH25MMS, HH24MMS, and LBS17H. Although the effect is not large it is noticeable and we believe it to be a significant discriminant. This would suggest that the density law flattens towards the centre of the clump (as in a Gaussian), although thus far such a requirement has only been determined for pre-collapse objects (e.g. Ward-Thompson et al. 1994). Future higher-resolution observations are clearly necessary to determine the density variation in the inner regions of these clumps.

Investigation on dummy data showed that the effect of fitting a single component model to a two component source (i.e. main component plus 'ridge') was to produce a behaviour in the opposite sense to that observed. The one object where a power law seems to fit reasonably well (SSV63) has a less pronounced peak on the map (Fig. 2) than the others.

5 DISCUSSION

5.1 Dust temperatures

From simple isothermal greybody modelling the derived dust temperatures in LBS23 are generally consistent with those derived from HCO$^+$ and NH$_3$ observations except in the case of HH24MMS, which yields a low dust temperature (Table 2). As

mentioned above, Chini et al. (1983) attribute this to an enhanced absorption coefficient. However, it should be noted that greybody fitting of the spectral energy distribution yields more accurate results as with enough data, the emissivity and its frequency dependence may be constrained in addition to the temperature (e.g. Ward-Thompson et al. 1995).

The dust temperatures tend to be rather lower than the CO-derived temperatures, which, on account of the very high CO optical depth, are likely to refer to the outer parts of the cloud. Although external heating of these outer parts therefore seems likely, it should be noted that the temperatures estimated for the ridges of LBS17 and LBS18 show little or no evidence of it. This fact indicates that the majority of the dust emission arises from the cold interior of the cores observed here.

5.2 Comparison with protostellar models

The canonical protostellar collapse model of Shu (1977) predicts inside-out collapse in an isothermal spherical envelope, leading to a density distribution with a power law of index –1.5 in the collapse region while outside it the index has the isothermal value of –2.0. The effect of magnetic fields and/or rotation will obviously complicate this simple picture. For example, the simulations of Crutcher et al. (1994), which include the effects of magnetic fields and ambipolar diffusion, indicate modifications of these laws to –1.3 and –1.7. Flattening would be expected leading to elongation in projection onto the plane of the sky.

The observations of the clumps do indeed reveal elongation which is particularly evident at 450 μm where the 8 arcsec beamwidth of the telescope is equivalent to 3200 AU. However, HH25MMS, HH24MMS and LBS18 are elongated in the direction of the filamentary structure in which they are embedded, suggesting perhaps that they might be prolate. In SSV63 and LBS17H the elongation appears to be perpendicular to the filaments.

When the observable extent of a source is not much greater than the beamwidth it is perhaps invidious to seek to distinguish between Gaussians and power laws. The central regions of the clumps can be fitted by Gaussians. It is hard to separate wing emission from a clump from emission due to the embedding filament. It is clear that, if the densities are interpreted as power law distributions, the power law indices vary with direction. The indices lie in the range –0.7 to –1.2 in the direction of elongation and –1.1 to –1.7 perpendicular to it. These values have been derived assuming an $r^{-0.3}$ temperature dependence. If the clumps were taken to be isothermal their magnitude would increase by about 0.3. Given that in the central regions Gaussians are somewhat favoured anyway, the least that can be said is that the results do not agree very well with the simple Shu model.

Questions pertinent to our results include: (a) are the cores oblate or prolate?, and (b) what has led to their orientation relative to the filaments in which they are embedded? While a number of papers have been published examining the fragmentation of filaments (e.g. Fiege & Pudritz 2000; Nakajima & Hanawa 1996), few have attempted to analyze the structure of the fragments and in particular look at the issue of prolate or oblate cores. However, Bonnell, Bate & Price (1996; hereafter BBP) have performed computer simulations of the dynamic evolution of initially prolate, magnetic field- and rotation-free filaments into protostars, which may be usefully related to our observations. The evolution depends primarily on the ratios of the Jeans radius to the minor and major axes of the filament, and they show that under certain conditions it is possible to produce an oblate core embedded within a prolate condensation.
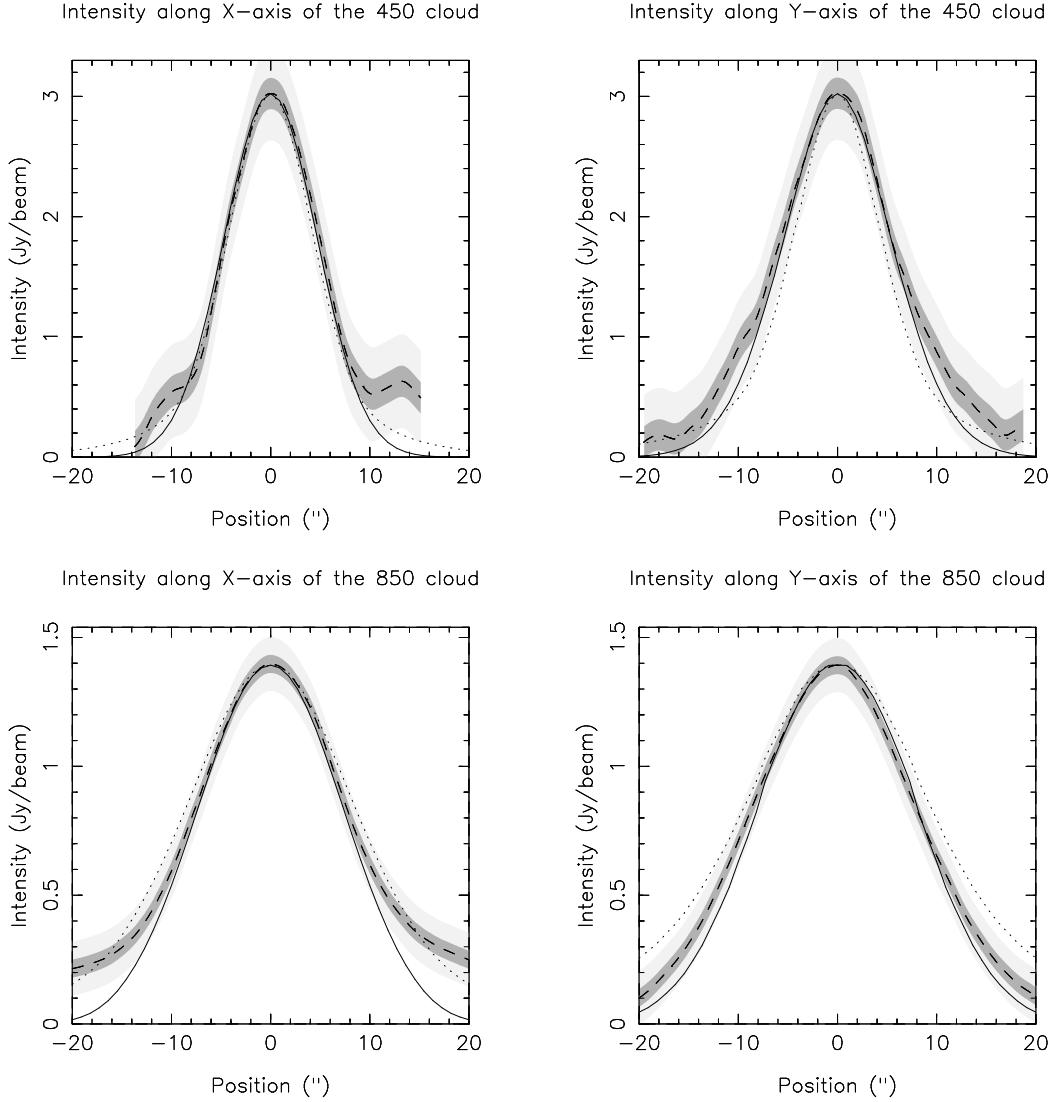
Figure 5. Cuts along the major and minor axes of LBS17H. The solid and dotted lines are respectively the modelled results from a Gaussian density distribution and a power law distribution. The dashed lines are cuts taken from Fig. 3. The strips are the 1σ and 3σ noise levels (from Fig. 3). The beamsizes used were 8 arcsec for 450 μm and 15 arcsec for 850 μm.

BBP give arguments to suggest that rotation would be unlikely to modify hugely these results. However, despite the claims of BBP, it is likely that magnetic fields may do so although their effects would depend on the field strength, direction and the Alfvén speed. For example, if the field lines were perpendicular to the axis of the filament then collapse across the field lines towards a single object might be inhibited on dynamical timescales, resulting in a string of individual cores which each form a protostar.

Can these theoretical considerations be related to our observations? First, we note that the effect of projecting both prolate and oblate object onto the plane of the sky is to decrease their apparent asymmetry. Both the filaments and the envelopes are, on average, more asymmetric than they appear. Second, the typical core size of a few $\times 10^3$ au is similar to the scale of the flattened structures in BBP's simulations. Thirdly, like LBS23 and NGC2024, LBS17 and LBS18 both have an elongated filamentary structure with protostellar cores appearing to form as a result of fragmentation along their length. Within the framework of BBP's simulations, their original filamentary structure was sufficiently massive that fragmenta-

tion has occurred along their length, as may have also happened in LBS18 (see Fig. 4). One would therefore expect that the condensations in these objects should be regarded as BBP's 'intermediate' prolate objects aligned with the original filaments.

HH25MMS, HH24MMS and LBS18S are elongated in the direction of the filamentary structure in which they are embedded, suggesting perhaps that they might indeed be prolate 'intermediate' cores which form after fragmentation of a prolate filament (BBP). But in SSV63 and LBS17H the elongation appears to be perpendicular to the filaments – within the framework of BBP's analysis they would be oblate 'ultimate' cores. Both these cores are observed at the ends, rather than centres, of filaments, however. Could it be that they have 'swallowed' all the material on one side of them? However, LBS18S is also observed at the end of a filament, but is elongated along the filament.

As there is evidence of star formation all along LBS23 it seems likely that protostars have sufficient time to form within the intermediate envelopes. Their mutual attraction could lead finally to a stellar cluster – not BBP's merging into a single object

which results from the symmetry of their initial starting conditions. BBP also note that the initial conditions require the accumulation of many Jeans masses in a time much shorter than the dynamic time scale, which might be achieved, for example, by cloud-cloud collisions, as proposed for the formation of the filament TMC1 by Little et al. (1978).

6 CONCLUSIONS: SEARCHING FOR PROTOSTARS

Searching LBS cores with SCUBA is a powerful method for detecting protostellar candidates in the Orion clouds. Several new ones have been discovered in very little observing time. On the simplest interpretation the clumps observed have masses (in the 15 arcsec beam) varying from a few (SSV59, SSV63, HH26) to 50 (HH24MMS) solar masses. Of the newly detected sources SSV59 and HH26IR are probably Class I objects, while LBS17H is a new Class 0 source. LBS18S has no near-infrared, IRAS or radio source, nor does it appear to have an outflow and so it is very young, perhaps pre-protostellar. Further studies of these objects, e.g. by interferometry, are required to confirm their evolutionary status.

One (LBS18) out of the 4 small LBS cores shows evidence of a protostellar clump of several solar masses. There are two in LBS17 (including the 1300 μm source of Launhardt et al. 1996) and several in LBS23. On the basis of present limited observations (4 small LBS cores, 2 large LBS cores) the ratio of 'protostellar' clump mass to the total virial mass of the filament does seem not very different for large or small cores – but the statistics are not good. A proper census of the LBS cores, in which both small and large cores are mapped in their entirety, feasible with SCUBA, will allow a mass spectrum of these clumps to be determined. The next obvious step is to carry out a wide field, unbiased survey of L 1630 to determine the mass distribution on 15-arcsec scales.

ACKNOWLEDGMENTS

REFERENCES

André P., Ward-Thompson D., Barsony M., 1993, ApJ, 406, 122
Bonnell I.A., Bate M.R., Price N.M., 1996, MNRAS, 279, 121 (BBP)
Bontemps S., Ward-Thompson D., André P., 1996, A&A, 314, 477
Chandler C.J., Carlstrom J.E., 1996, ApJ, 466, 338
Chandler C.J., Moore T.J.T., Emerson J.P., 1992, MNRAS, 256, 369
Chandler C.J., Richer J.S., 2000, ApJ, 530, 851
Chini R., Krugel E., Haslam, C.G.T., Kreysa E., Lemke R., Reipurth B., Sievers A., Ward-Thompson D., 1993, A&A, 272, L5
Choi M., Panis J-F., Evans N.J., II, 1999, ApJS, in press
Crutcher R.M., Mouschovias T.Ch., Troland T.H., Ciolek G.E., 1994, ApJ, 427,839
Davis C.J., Ray T.P., Eislöffel J., Corcoran D., 1997, A&A, 324, 263
Dent W.R.F., Matthews H.E., Walther D.M., 1995, MNRAS, 277, 193
Fiege J.D., Pudritz R.E., 2000, MNRAS, 311, 105
Gibb A.G., 1999, MNRAS, 304, 1
Gibb A.G., Davis C.J., 1997, in Malbet F., Castets A., eds, Poster Summaries, IAU Symp. 182, Low Mass Star Formation – from Infall to Outflow. Université Joseph Fourier, Grenoble, p. 120
Gibb A.G., Davis C.J., 1998, MNRAS, 298, 644
Gibb A.G., Heaton B.D., 1993, A&A, 276, 511 (GH93)
Gibb A.G., Little L.T., 1998, MNRAS, 295, 299 (GL98)
Gibb A.G., Little L.T., 2000, MNRAS, 313, 663
Gibb A.G., Little L.T., Heaton B.D., Lehtinen K.K., 1995, MNRAS, 277, 341 (Paper I)
Haschick A.D., Moran J.M., Rodríguez L.F., Ho P.T.P., 1983, ApJ, 265, 281
Hildebrand R.H., 1983, QJRAS, 152, 1
Holland W.S., Robson E.I., Gear W.K., Cunningham C.R., Lightfoot J.F., Jenness T., Ivison R.J., Stevens J.A., Ade P.A.R., Griffin M.J., Murphy J.A., Naylor D.A., 1999, MNRAS, 303, 659
Huard T.L., Sandell G., Weintraub D.A., 1999, ApJ, 526, 833
Lada C.J., 1991, in Lada C.J., Kylafis N.D., eds, The Physics of Star Formation and Early Stellar Evolution, Kluwer, Dordrecht, p. 329
Lada E.A., Bally J., Stark A.A., 1991, ApJ, 368, 432
Launhardt R., Mezger P.G., Haslam C.G.T., Kreysa E., Lemke R., Sievers A., Zylka R., 1996, A&A, 312, 569
Lis D.C., Carlstrom J.E., Phillips T.G., 1991, ApJ, 370, 583
Lis D.C., Menten K.M., Zylka R., 1999, ApJ, 527, 856
Little L.T., Riley P.W. Macdonald G.H., Matheson D.N, 1978, MNRAS, 183, 805
Little L.T., Gibb A.G., Heaton B.D., Ellison B.N., Claude S.M.X., 1994, MNRAS, 217, 649
Mauersberger R., Wilson T.L., Mezger P.G., Gaume R., Johnston K.J., 1992, A&A, 256, 640
Menten K.M., Walmsley C.M., Mauersberger R., 1987, in Appenzeller I., Jordan C., eds, Circumstellar Matter, Reidel, Dordrecht, p.179
Mezger P.G., Sievers A.W., Haslam C.G.T., Kreysa E., Lemke R., Mauersberger R., Wilson T.L., 1992, A&A, 256, 631
Nakajima Y., Hanawa T., 1996, ApJ, 467, 321
Phillips R.R., Little L.T., 2000, MNRAS, 317, 179
Scoville N.Z., Kwan J., 1976, ApJ, 214, 488
Shu F.H., 1977, ApJ, 214, 488
Testi L., Sargent A.I., 1998, ApJ, 508, L94
Verdes-Montenegro L., Ho P.T.P., 1996, ApJ, 473, 929
Visser A.E., Richer J.S., Chandler C.J., Padman R., 1998, MNRAS, 301, 585
Ward-Thompson D., Scott P.F., Hills R.E., André P., 1994, MNRAS, 268, 276
Ward-Thompson D., Chini R., Krügel E., André P., Bontemps S., 1995, MNRAS, 274, 1219
Zhou S., Evans N.J., II, Güsten R. Mundy L.G., Kutner M.L., 1991, ApJ, 372, 518

APPENDIX A: DUST RADIATIVE TRANSFER MODEL

Our radiative transfer model is a simple modification to the axisymmetric molecular line transfer code of Phillips & Little (2000) to cope with dust continuum emission.

The emissivity, E_ν, of a small element i is written as

$$E_{\nu,i} = \kappa_{\nu,i} \frac{2h\nu^3}{c^2(e^{\frac{h\nu}{kT_d}} - 1)} \tag{A1}$$

where the dust is at a temperature T_d. The cloud to be modelled is split into geometrical subsections. The geometrical subsections chosen for the cloud are a series of stacked concentric rings. Each subsection is assigned a temperature and a molecular hydrogen density according to the desired model. For any desired line of sight the positions of the intersections of the line of sight with the boundaries of the subsections are then calculated. It is then possible to integrate the emission along the line of sight simply by adding up the contributions from each segment on the line of sight (Δl_i) according to

$$I_\nu = \sum_{i=1}^{n} E_{\nu,i} \Delta l_i e^{-\sum_{j=1}^{i} \tau_{\nu,j}} \tag{A2}$$

where $E_{\nu,i}$ and $\tau_{\nu,j}$ are the emissivities and optical depths for segment i (or j) respectively.

The beam-averaged emission is computed by taking a grid of positions over the beam, calculating the emission from each and summing the results with appropriate weightings. For all the modelling that follows the beam is assumed to be a perfect Gaussian. Whilst this is a good assumption for the 850 μm data the JCMT beam deviates from a perfect Gaussian at 450 μm due to imperfections in the dish. Observations of Uranus showed that the beam had a substantial 'error' component containing $\sim$50 per cent of the power and spread over a 50 arcsec-diameter region. However, although the precise shapes of the 450 μm cuts may be slightly inaccurate (mostly at the lower levels), the difference is almost certainly not enough to significantly affect our results.

Two different models for the molecular hydrogen distribution were tested. The first is a power law model of the form

$$n_{H_2} = c_n D^{-d_n - e_n} \left[\cos\left(\frac{\pi}{2} \left(\frac{2|\theta|}{\pi} \right)^m \right) \right]^2 \qquad (A3)$$

where $D = R/R_{in}$, $\theta = \tan^{-1}\left(\frac{z}{r} \right)$ and r and z are the cylindrical co-ordinates of the position of interest in the cloud with the z-axis being the axis of symmetry in the cloud and r the distance from the axis, while R refers to the distance from the cloud centre measured in parsecs. The z axis is taken to lie in the plane of the sky. Choosing appropriate values of d_n and e_n enables the power law dependence to vary with direction, thus allowing an elongated cloud to be described. By changing the sign of e it is possible to model either a prolate or an oblate cloud. Although such a description has the major advantage of enabling easy comparisons with various predictions for the power law in each direction it is difficult to obtain smooth elliptical contours of equal density. It is necessary to give the value of c_n for a position, R_{in}, close to the centre of the cloud rather than at the outer edge as many authors have done (e.g. Little et al. 1994) since specifying the density at the outer edge causes the two different power laws to give two different density values at the cloud centre. The apparently odd angular variation simply produces nicely oval contours, with m chosen between 1.3 and 1.5 for prolate clouds and between 0.7 and 0.8 for oblate ones. We also tried using a Gaussian distribution of the form

$$n_{H_2} = c_n \exp\left(-\left[\left(\frac{r}{d_n} \right)^2 + \left(\frac{z}{e_n} \right)^2 \right] \right) \qquad (A4)$$

where r and z are as described above for the power law. The parameters d_n and e_n enable the size of the Gaussian (and hence the cloud) to be specified.

The temperature distribution has been assumed to be spherically symmetric and varies according to

$$T_K = a_T R^{0.3} + b_T R^{-0.3} \qquad (A5)$$

where R is the distance to the centre of the cloud measured in parsecs. This distribution, which crudely represents a cloud that may be both internally and externally heated, is taken from the results of Scoville & Kwan (1976) which assumes that $\beta = 2$. GL98 applied this formula to HH24MMS and HH25MMS in LBS23 for modelling C I and $C^{18}O$. In principle the temperature variation with distance from the centre should be different along the two axes of the flattened model core. However, Scoville & Kwan (1976) show that the optical depth probably has a greater effect on the temperature fall off than the density law, and thus for simplicity we retain a spherically-symmetric temperature distribution.

For all models a cloud consisting of 60 cylinders and 60 disks (i.e. a total of 3540 rings) was used with both the disks and cylinders packed closer together near the centre of the cloud (this enables the rapid changes of the power laws near the centre of the cloud to be modelled without large jumps in the parameter values from one ring to another). The cylinders have an outer radius of 0.05 pc and the disks extend out to a distance of 0.05 pc above and below the centre of the cloud. The exact choice of this distance does not affect the results for the Gaussian models. However, power law models are affected to varying degrees depending upon the steepness of the power law used. For steep power laws the cross-section shape remains approximately the same with only a 10 per cent change in c_n when the radius is increased by a factor of 4. For the shallow power law the changes are much bigger. For the worst case increasing the radius of the cloud by a factor of 4 leads to significantly higher emission at the edge of the cross sections, particularly for the 450 μm crossection. This can be corrected by making the power law a little steeper (0.1 extra in each direction) with a 60 per cent increase in c_n.

In order to model the beam correctly for the rapid changes in the centre of the cloud a total of up to 55$\times$55=3025 lines of sight are distributed across the beam. This number was determined by trying progressively larger numbers of lines of sight for each model until the cross-sections stopped changing.

The program initially calculates the intensity only for the central point in the cloud and then, by adjusting the values of b_T (in equation A5) and c_n (in equations A3 & A4), it fits the peak temperatures in the 450 and 850 μm maps. Once the peaks are fitted correctly a map is produced and then the four cuts are compared with the telescope data.

With power laws there is usually a problem with deciding where to place an inner cut off R_{in} (necessary to prevent a singularity at the centre of the cloud). We have used 0.001 pc here, although there are only minor changes in the results if this is increased or decreased by a factor of 5. This is because the extremely small area in the centre of the cloud has little affect on the total emission over the beam.

There is also some question as to the precise form of the emissivity. The Hildebrand (1983) formula, which we have used here, proposes that in the long wavelength regime ($\lambda > 250\mu$m) the absorption coefficient at a frequency ν (GHz) is related to the molecular hydrogen density n_{H_2} (cm^{-3}) by

$$\kappa_\nu = \frac{2n_{H_2}}{1.2 \times 10^{25}} \left(\frac{\nu}{750} \right)^2 \qquad \mathrm{cm}^{-1} \qquad (A6)$$

Others (e.g. Visser et al. 1998 and Testi & Sargent 1998) have recently suggested that lower values for β may be more appropriate. We tested this by using the relationship suggested by Testi & Sargent (1998) of $\kappa_\nu = \frac{2n_{H_2}}{9.6 \times 10^{25}} \left(\frac{\nu}{230} \right)^{1.1}$ cm^{-1} in place of equation A6, where as before ν is in GHz and n_{H_2} is in cm^{-3}. However, as mentioned in the text, the precise choice of emissivity law does not significantly affect the results (other than the magnitude of the temperature and density).

This paper has been produced using the Royal Astronomical Society/Blackwell Science LaTeX style file.